

**Dieses Dokument ist eine Zweitveröffentlichung (Verlagsversion) /
This is a self-archiving document (published version):**

Axel Renner, Uwe Marschner, Wolf-Joachim Fischer

**A new imaging approach for in situ and ex situ inspections of
conductive fiber-reinforced composites by magnetic induction
tomography**

Erstveröffentlichung in / First published in:

Journal of Intelligent Material Systems and Structures. 2014, 25(9), S. 1149 - 1162 [Zugriff am:
12.08.2019]. SAGE journals. ISSN 1530-8138.

DOI: <https://doi.org/10.1177/1045389X13507349>

Diese Version ist verfügbar / This version is available on:

<https://nbn-resolving.org/urn:nbn:de:bsz:14-qucosa2-356194>


„Dieser Beitrag ist mit Zustimmung des Rechteinhabers aufgrund einer (DFGgeförderten) Allianz- bzw. Nationallizenz frei zugänglich.“

This publication is openly accessible with the permission of the copyright owner. The permission is granted within a nationwide license, supported by the German Research Foundation (abbr. in German DFG).

www.nationallizenzen.de/

A new imaging approach for in situ and ex situ inspections of conductive fiber–reinforced composites by magnetic induction tomography

Axel Renner, Uwe Marschner and Wolf-Joachim Fischer

Journal of Intelligent Material Systems and Structures
2014, Vol. 25(9) 1149–1162
© The Author(s) 2013
Reprints and permissions:
sagepub.co.uk/journalsPermissions.nav
DOI: 10.1177/1045389X13507349
jim.sagepub.com


Abstract

Fiber-reinforced plastics for industrial applications face constantly increasing demands regarding efficiency, reliability, and economy. Furthermore, it was shown that fiber-reinforced plastics with tailored reinforcements are superior to metallic or monolithic materials. However, a trustworthy description of the load-specific failure behavior and damage evolution of composite structures can hardly be given, because these processes are very complex and are still not entirely understood. Among other things, several research groups have shown that material damages like fiber fracture, delamination, matrix cracking, or flaws can be discovered by analyzing the electrical properties of conductive composites, for example, carbon fiber–reinforced plastics. Furthermore, it was shown that this method could be used for structural health monitoring or nondestructive evaluation. Within this study, magnetic induction tomography, which is a new imaging approach, is introduced in the topic of nondestructive evaluation of carbon fiber–reinforced plastics. This non-contacting imaging method gains the inner spatial distribution of conductivity of a specimen and depicts material inhomogeneity, like damages, not only in two-dimensional images but also in three-dimensional images. Numerical and experimental investigations are presented, which give a first impression of the performance of this technique. It is demonstrated that magnetic induction tomography is a promising approach for nondestructive evaluation. Potentially, it can be used for fabrication quality control of conductive fiber–reinforced plastics and as a structural health monitoring system using an integrated or superficially applied magnetic induction tomography setup.

Keywords

Magnetic induction tomography, carbon fiber–reinforced plastics, nondestructive testing, structural health monitoring

Introduction

Fiber-reinforced plastics (FRPs) are excellent materials for economic manufacturing since they enable a weight saving construction with tailored and customized reinforcements while providing high specific strength and stiffness at once. However, the application fields those having the most benefit of this lightweight construction technique—such as aerospace—have mostly high safety requirements at the same time.

However, it is a problem to give a trustworthy description of load-specific failure behavior and damage evolution of composite structures. Consequently, the condition of FRPs needs to be inspected regarding failures or damages during manufacturing as well as in the field with most care to guarantee quality and structural integrity and to avoid catastrophic failures.

Furthermore, a possible prediction of the remaining service life of composite parts could save maintenance costs. So, in addition to damage detection, more

detailed information of the damage like localization, quantification, and classification as well as an estimation of the severity of defects are essential to gain an airtight diagnostic statement. For this purpose, several nondestructive evaluation (NDE) methods have been established in the last decades, which are basically ultrasonic testing (C-scan and pulse echo), scanning acoustic microscopy, X-ray inspection (two-dimensional (2D) radiosopic transmission imaging and three-dimensional (3D) computed tomography), neutron radiography, thermography, lamb wave

Institute of Semiconductors and Microsystems, Technische Universität Dresden, Dresden, Germany

Corresponding author:

Axel Renner, Institute of Semiconductors and Microsystems, Faculty of Electrical and Computer Engineering, Technische Universität Dresden, Nöthnitzer Straße 64, 01062 Dresden, Germany.
Email: axel.renner@tu-dresden.de

sensing, near-field microwave, and so on (Li, 2012). It was found that each NDE method has own assets and drawbacks with regard to characterization, flaw detectability, and applicability, and that a single NDE method might not be able to address all requirements at the same time. For instance, ultrasonic testing is a reliable and frequently used NDE method but cost-intensive equipments and well-trained operators are necessary. The same applies to scanning acoustic microscopy or X-ray inspection where the latter additionally involves ionizing radiation, which is complex to handle. The mentioned NDE methods often require further expenditures, like device calibration, which make a quick, portable, and easy-to-use in-service inspection difficult or impossible. This is, for instance, the case in ultrasonic testing where an acoustic couple medium like water or gel might be necessary.

Nevertheless, it was already proven that there is a relationship between the electrical properties (conductivity and permittivity) and mechanical (strain) or structural integrity (damages) of conductive FRPs, so that the composite itself can be used as a sensor (self-sensing) in NDE or structural health monitoring (SHM) systems (Abry et al., 2001; Böger et al., 2008; Kupke et al., 2001; Ngabonziza et al., 2010; Schüler et al., 2001; Todoroki, 2008; Yang et al., 2007). Such conductive composites are for instance materials like carbon fiber-reinforced plastics (CFRPs) or glass fiber-reinforced plastics (GFRPs) doped with conductive particles like carbon nanotubes or carbon dust (Kostopoulos et al., 2009). Against this background eddy current testing NDE—which is already known for several decades as a low cost, contactless, easy to use and widely used industrial NDE method—was developed with regard to the specifics of CFRPs, and its potential in flaw detection and composite characterization was effectively demonstrated. One drawback of this method is that the detection of defects is primarily restricted to surface and near-surface flaws. Anyway, spatial information about the spread of damages within a composite part would be supplementary valuable in advanced diagnosis evaluation of the damage condition.

Most of the mentioned NDE methods like eddy current testing are not able to provide spatial information except expensive tomography methods like computed tomography. Against this background, electrical resistance tomography (ERT) (Baltopoulos et al., 2010) was developed as a cost-efficient alternative to conventional tomography methods, and it was demonstrated that damages in CFRPs can be exposed regarding size and position. Nevertheless, ERT requires a galvanic coupling with the specimen's boundary so this method seems to be impractical for NDE in industrial applications.

Within this study, magnetic induction tomography (MIT) as a novel, contactless, and inexpensive imaging approach for NDE of conductive FRPs is presented,

which combines the advantages of conventional eddy current testing and tomography methods. Compared to conventional eddy current testing methods (Lane et al., 1991), MIT is able to produce 3D images of the interior spatial distribution of complex conductivity of a test object and hence make a 3D representation of material damages possible. MIT employs an externally arranged annular coil assembly of several excitation and detection coils. The excitation coils are driven by sinusoidal currents. They produce a primary time-varying magnetic field, which induces eddy currents inside the specimen at various locations. These eddy currents in turn produce a secondary magnetic field, which is linked to the spatial distribution of conductivity. It is measured by the detection coils.

Apart from some industrial MIT applications (Ma et al., 2006; Peyton et al., 1995; Soleimani et al., 2006b; Wei and Soleimani, 2012c; Yin et al., 2011), MIT research was predominantly done with focus on biomedical applications. Most of this study was merely done in numerical investigations or physical experiments, which utilize phantom assemblies. Moreover, most of those investigations produced only 2D conductivity images with low resolution (Wei et al., 2012). Since the image quality rapidly decreases with noisy and distorted signals following the human body's poor and extremely inhomogeneous electrical conductivity, no in vivo image of the human body could be produced so far (Griffiths, 2001).

However, some fundamental and promising features were investigated within the scope of medical imaging beforehand. For example, Gürsoy and Scharfetter (2010) discussed anisotropic imaging and presented an adapted reconstruction approach. Furthermore, Soleimani and Lionheart (2006a) showed that the image quality could be notably improved with a nonlinear solver if precise measurements are given. This nonlinear solver was tested with experimental data concerning industrial aspects with regard to molten metal flow visualization (Soleimani et al., 2006b). Both anisotropic and nonlinear reconstruction approaches were not combined yet. A planar MIT system using adverse sensor arrays was presented in Watson et al. (2005). A time-resolved (four-dimensional (4D)) image reconstruction of moving objects was investigated in physical experiments by Wei and Soleimani (2012a). It was found that one can make use of temporal correlations between reconstructed frames to improve temporal resolution and spatial resolution.

The goal of this study is to demonstrate that MIT is basically applicable in NDE of CFRPs. Therefore, it is necessary to prove that MIT is also able to display defects in such thin structures as composite parts since this was not shown so far. If this is proven, one can suppose a much better image quality with higher spatial resolutions as achieved in biomedical imaging. The improvement is based on the high signal-to-noise ratio

(SNR) that can be assumed since CFRPs have much greater (approximately four to five orders) conductivity than biological tissues. In addition, CFRPs show a quite simple anisotropic conductivity distribution in comparison to the human body. Motivated by this, the ambition of the NDE approach presented in this study is to utilize the MIT tool set to attain diagnostic information about FRP damage conditions in terms of localization, quantification, and classification of material damages or failures.

To reach this, the basics of MIT imaging, the mathematical background as well as the measurement methods will be explained at first, and finite element (FE) methods are applied in order to process measurements. In the second part of this article, the specifics using MIT in NDE of CFRP parts will be discussed in numerical studies and options to increase image quality and spatial resolution investigated. Therefore, 2D imaging methods are utilized to setup 3D methods. Finally, the method will be tested in experimental 3D imaging. The methods and primary results made in this study will be used for the design of a SHM system, which utilizes magnetic induction methods in future study.

Methods

As mentioned above, on one hand, experimental MIT imaging needs experimental equipment for data collection, and on the other hand, it needs signal processing techniques for the mathematical solution of an inverse eddy current problem.

Methods for image reconstruction

Image reconstruction in MIT takes three major steps. At first, a forward model has to be solved, which is discretized and linearized in a second step. The forward model provides a database, which is used for solving a nonlinear inverse problem subsequently (Merwa et al., 2005).

The goal of the forward problem is to calculate a prediction of the electromagnetic fields and the resulting voltages induced in the detection coils. This is done using Maxwell's equations and a priori known conductivity distribution. The solution of the corresponding inverse eddy current problem gives an approximation of an unknown conductivity distribution from a certain set of measurements. For this purpose, the assumption is made that the nonlinear forward problem can be represented with a system of linear equations. In doing so, one can write

$$S \cdot \sigma_0 = V_0 \quad (1)$$

in which the vector σ_0 is an initial guess of the conductivity distribution for instance that of an undamaged

specimen. The vector V_0 represents the measured voltages, which one would get with a specimen having the initial conductivity distribution. Both quantities are assumed to be a priori known and are linked by a sensitivity matrix S . Hence, the specimen to be imaged is discretized into finite image elements (the image pixel/voxel). The measurement sensitivity S_V to a conductivity change $\partial\sigma_V$ in the image element V is

$$S_V = \frac{\partial V_{ij}}{\partial \sigma_V} \quad (2)$$

where the resulting change in the induced voltages ∂V_{ij} is measured with excitation coil i and detection coil j . The coefficients of the sensitivity matrix S are then computed for all image elements and coil combinations by equation (2) (Gürsoy and Scharfetter, 2009).

In the inverse problem, now the conductivity distribution of the specimen to be tested is unknown and the system of equations must be inverted to get the reconstructed conductivity σ_{rec} with the measured voltages V_m

$$\sigma_{rec} = S^{-1} V_m \quad (3)$$

In view of the fact that the inverse problem is ill-posed as well as sensitive to noise and measurement errors, appropriate stabilization of the solution is necessary. Within this study, Tikhonov regularization for dynamical imaging was applied (Merwa et al., 2005), which can be written as

$$\Delta\sigma_{rec} = (S^T S + \lambda R)^{-1} S^T \Delta V_m \quad (4)$$

and which calculates an approximation of the conductivity change $\Delta\sigma_{rec}$ between two different states, for instance, healthy and damaged state of a composite part. In this case, the vector ΔV_m stands for the difference between the voltages one obtains with the undamaged and damaged specimens. The regularization matrix R multiplied by a regularization parameter λ gives the regularization term, which smoothes instabilities of the solution. Within this study, R is an identity matrix. There are methods for an automatic determination of λ , for instance, generalized cross validation (Hanke and Hansen, 1993). Due to our a priori knowledge of the damage, λ was chosen by visual inspections of the reconstructed images to fasten the measuring process.

Measurement setup

As already mentioned, MIT is based on eddy current testing. Typically, excitation coils are used for stimulation of the specimen at different positions by generating primary magnetic fields. The secondary fields resulting from eddy currents induced within the sample are

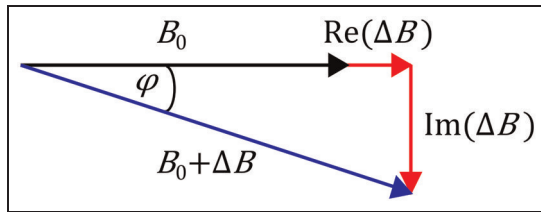


Figure 1. Phase diagram of the primary and secondary magnetic field.

picked up with detection coils. The relation between primary and secondary fields can be seen in the phase diagram in Figure 1. The detection coil measures the primary field B_0 of the excitation coil as well as the secondary field ΔB , which is superimposed to B_0 with a phase shift φ of the complete magnetic field $B_0 + \Delta B$ relative to B_0 . The secondary field ΔB comes from the induced eddy currents of the specimen. ΔB is complex having a real part and an imaginary part, which contain information about the permittivity and conductivity of the specimen (Griffiths, 2001). Within this study, the imaginary part of ΔB is utilized to measure conductivity changes. So, to distinguish between the real and imaginary parts of ΔB , phase-sensitive detection was employed using a dual-phase lock-in amplifier (HF2LI; Zurich Instruments).

In MIT, the magnitudes of primary fields are usually several orders larger than those of secondary fields. Consequently, it is difficult to detect the small secondary fields against a strong primary background signal. Hence, compensated coil configurations of excitation and detection coils are commonly used in MIT, which

significantly decrease the sensitivity of the detection coils to the primary fields of the excitation coils. Therefore, the detection coils are arranged perpendicular to the excitation coils (Watson et al., 2005).

Thus, a sensor array made of printed circuit boards (PCBs) was built having six excitation and seven detection coils (see Figure 2). Each coil has four turns with an external diameter of 12 mm. The distance between excitation and detection coils is 4.6 mm. The distance between the surface of the specimen and the excitation coils is 10 mm. The specimen has a size of 110 mm \times 80 mm \times 5.6 mm.

A sinusoidal excitation was generated and amplified subsequently using the internal signal generator of the lock-in amplifier and a power amplifier. A reference signal was derived from electric shunts for monitoring the excitation currents. Multiplexer and demultiplexer provide appropriate selections of coils and shunts. To conduct measurements at different positions, the specimen mounting was shifted horizontally with a linear guide unit driven by a stepper motor. The control of the overall assembly and storage of measurement results was done using MATLAB running on a PC. A schematic representation of the MIT setup is given in Figure 3.

Setting up the database/forward model

For computation of the forward problem or rather the sensitivity matrix, a FE model was created, which emulates the experimental MIT system and the measuring procedure, which is discussed and described next. Therefore, the same geometry and dimensions of the experimental arrangement of coils and CFRP sample

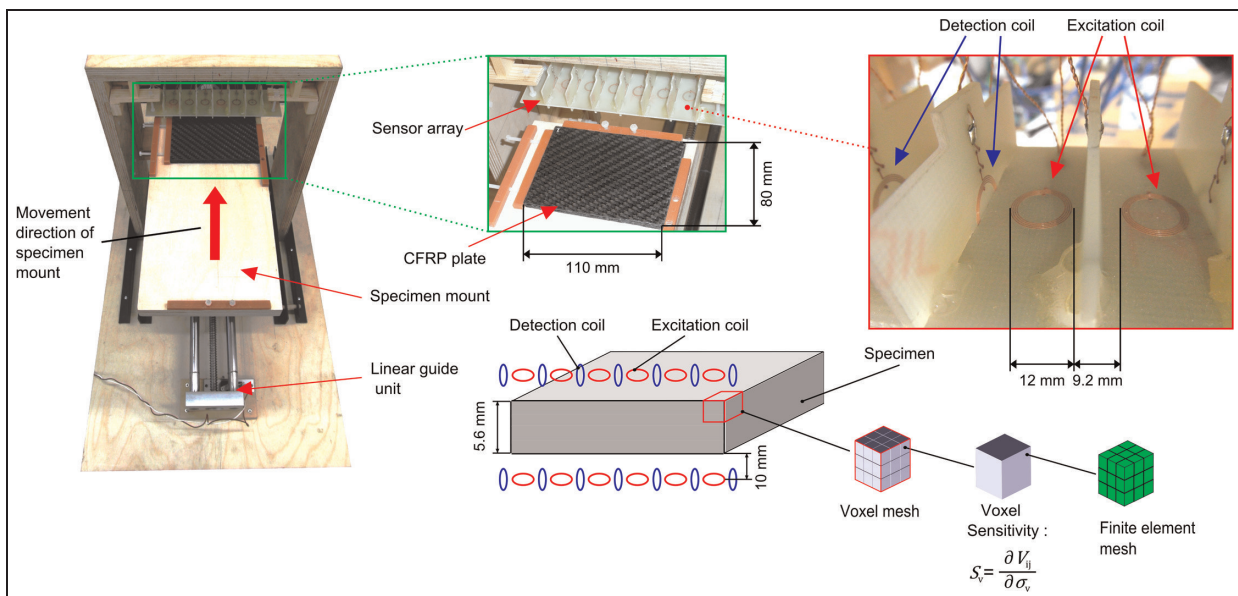


Figure 2. Photographs and illustration of the 3D measurement setup, arrangement of coils, and CFRP plate. CFRP: carbon fiber–reinforced plastic; 3D: three-dimensional.

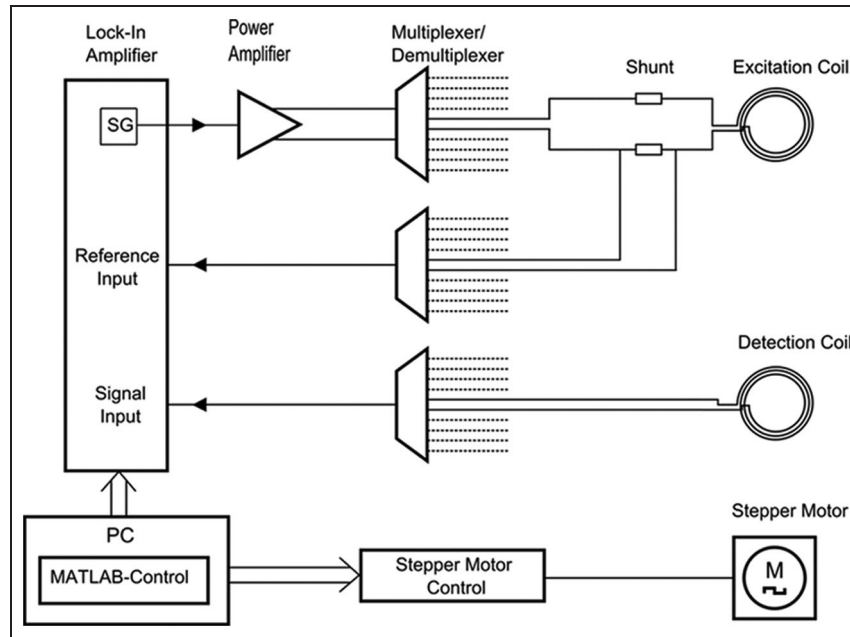


Figure 3. Schematic representation of the MIT setup for contactless 3D imaging of conductive FRPs with lock-in amplifier. MIT: magnetic induction tomography; 3D: three-dimensional; FRP: fiber-reinforced plastic.

were modeled and meshed afterward using ANSYS Emag (236'ers) edge elements. With the help of ANSYS, the initial field distribution is computed. This prerequisite is necessary for each new configuration. The computation of the FE forward model is very time-consuming. For this reason, this was done for 2D (x, z) imaging initially to setup 3D imaging (x, y, z) as described later. For 2D imaging, the specimen and all coils were modeled cross-sectional. The CFRP specimen was discretized into a regular hexahedral mesh having (1) 38,016 elements ($66 \times 48 \times 12$ elements) for 3D imaging and (2) 2640 elements (220×12 elements) for 2D imaging. The FE models for 2D as well as 3D imaging are shown in Figure 4. For the sake of clarity, only one sensor array (above the specimen) is depicted but the full model has also an identical sensor array below the specimen, as illustrated in Figure 2. The entire models including coils, specimen, and enclosing air were meshed with (1) 140,379 elements or (2) 54,610 elements and no special boundary conditions were applied. Every coil was shaped as a single turn. For each simulation, an excitation current of 1 A was employed. The forward calculations were performed with a conductivity of $\sigma_0 = 5 \times 10^4$ S/m. Thereby, an isotropic conductivity distribution of the CFRP sample was assumed. As already mentioned, CFRPs have an anisotropic conductivity distribution, which depends strongly on the alignment of the carbon fibers within the composite. Given that within this study, only an isotropic reconstruction solver was used this would mean that an anisotropic problem needs to be mapped in an isotropic model. This procedure can introduce

errors in the image reconstruction as already discussed in numerical investigations in Gürsoy and Scharfetter (2010). However, it was also shown that an isotropic perturbation, which is located in an anisotropic medium, can be already sufficiently reconstructed with an isotropic approach. In some cases, it can be reconstructed with even better image quality compared to reconstructions achieved with an anisotropic solver when the reference data set is generated by incorporating the unperturbed anisotropic conductivity distribution. Within this study, the same situation as in the citation mentioned above arises. The reference data set was measured with the CFRP reference sample as described in the following, which has, except the damage, the same anisotropic conductivity distribution as the device under test. The perturbations obtained in this study are also isotropic. Furthermore, the CFRP specimens were designed to develop approximately isotropic conductivities as described in the following. Hence, the sensitivity matrices used in this study were calculated by assuming an isotropic conductivity distribution.

An adjoint field method applying reciprocity theorem was used, which gives an approximation of the Jacobian matrix (Hollaus et al., 2003). Therefore, the electric field distribution was calculated for each excitation coil and detection coil. The entries of the sensitivity matrix followed from the inner product of both electric fields.

Having those sensitivity matrices gives two options for 3D imaging. One choice is to reconstruct the images based on the FE mesh for image reconstruction, which

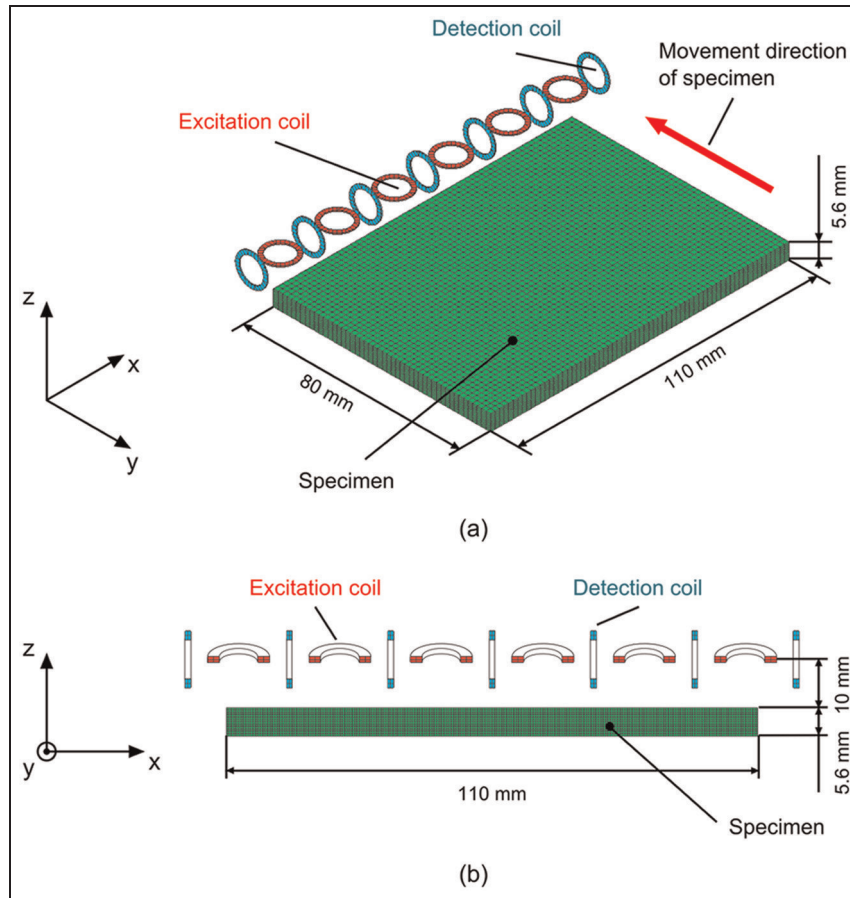


Figure 4. Image of the finite element model for computation of the sensitivity matrix for (a) 3D imaging and (b) 2D imaging. 3D: three-dimensional; 2D: two-dimensional.

Table 1. Model specifications used in numerical and experimental image reconstruction.

Imaging mode	Voxel/pixel dimensions	Resolution	Number of unknowns
2D	$2 \times 0.467 \text{ mm}^2$	$220 \times 12 \text{ Pixel}$	2640
3D	$5 \times 5 \times 1.4 \text{ mm}^3$	$22 \times 16 \times 4 \text{ Voxel}$	1408
	$1.667 \times 1.667 \times 0.467 \text{ mm}^3$	$66 \times 48 \times 12 \text{ Voxel}$	38,016

2D: two-dimensional; 3D: three-dimensional.

was used for eddy current computation. Another choice is to divide the FE mesh into a coarser imaging mesh. This reduces the number of unknowns of the set of linear equations and the spatial resolution. In the first case, one get an imaging mesh of $66 \times 48 \times 12$ voxel. For composing a coarser imaging mesh, each image voxel was built up of $3 \times 3 \times 3$ subvoxel or FE elements (see Figure 1). In this way, one gets 1408 image voxel. This imaging mesh has a resolution of four stacked image layers of 22×16 voxel, the 2D imaging mesh of 220×12 pixels. All model specifications are summarized in Table 1.

Measuring procedure

The data sets for the image reconstruction were recorded with the MIT setup described beforehand. To create the measurement vector ΔV , measurements from a reference and a damaged specimen were taken. Both were shifted horizontally beneath the sensor array by means of the linear guide unit in several equidistant steps. At every step, each excitation coil was activated sequentially. Only nearby detection coils were used for the measurements. In doing so, 6 (excitation coils) \times 2 (neighboring detection coils) = 12 measurements per step were performed. Since the experimental setup

provides only one sensor array, the specimens were swapped and measured again for two-sided data collection of the specimens.

Results and discussion

Discussion of MIT in NDE of CFRPs

Using MIT in nondestructive testing (NDT) of CFRPs implicates some specifics compared to other MIT tasks. For instance, CFRP parts are often thin. As a consequence, a much higher spatial resolution as reached so far is necessary to accomplish sufficient in-plane and depth-related information of the damage. In addition, an annular coil arrangement, which was used in the most MIT studies, is not applicable for geometries like plates.

Within this study, a planar MIT setup was used. Imaging with a sufficient spatial resolution is more difficult to achieve with planar MIT since there are just two directions of projections available (top and bottom of the plate), which can be used for the measurements instead of an annular MIT system, which provides cylindrically distributed direction of projections. Hence, the database given by a certain set of measurements using a planar MIT system will be mathematically more ill-posed than using an annular coil arrangement because a smaller number of independent measurements can be taken. However, for image reconstruction, it is more important to have independent measurements than just a high number of measurements because correlations between measurements add only redundant information to the image reconstruction. To overcome these difficulties, special attention needs to be paid about the way how measurements are taken.

Considering the planar MIT system, which is employed in this study, there are in general some options to increase the number of measurements. For instance, one could

- Increase the number of coils;
- Increase the number of coil combinations;
- Increase the number of horizontal shifts of the specimen mounting;
- Gather measurements at different frequencies.

Increasing the number of coils requires improved hardware and might not be an option in SHM applications since a 2D coil array might become too dense because of limited measuring space. The way in which the numbers of horizontal shifts of the specimen mounting and the choice of different excitation frequencies have also a positive effect on the image quality will be discussed in the following.

Simulation-based singular value decomposition of the sensitivity matrices

Increasing the number of equidistant shifts of the specimen mounting will not only increase the number of

measurements, which are available for image reconstruction, but also increase the measurement time. To increase the number of shifts, the step sizes of the horizontal shifts need to be decreased.

To what extent it is reasonable to take measurements with a smaller step size to improve the image quality but also accept an increase in the measurement time can be evaluated by the normalized singular values of the sensitivity matrix. Those can be calculated by the singular value decomposition $SVD(S'S)$ (Wei and Soleimani, 2012b).

To evaluate how a method is reasonable to improve the image quality, the singular values, which are above the noise level of the MIT system, are examined because the singular values below the noise level are truncated during regularization. These values do not contribute to the image reconstruction. Another option is to obtain the decay rate of the normalized singular values because a slower decay means that the inverse problem is less ill-posed (Soleimani, 2005).

To investigate the influence of different step sizes, several sensitivity matrices for 3D imaging at 1 MHz with 11, 13, 17, and 33 steps were calculated as well as their normalized singular values. Those step numbers imply a step size of the specimen mounting of 8, 6.6, 5, and 2.5 mm.

Figure 5(a) shows the normalized singular values for different numbers of steps for the MIT system used in this study. As can be seen from Figure 5(a) by assuming for instance 1% noise in the MIT system, there are just 161, 302, 402, and 453 singular values above the noise level using 11, 13, 17, or 33 steps. This means that decreasing the step size makes more singular values available for image reconstruction. Otherwise, one can see in Figure 5(a) that the decay rate of the singular values decreases with higher number of steps (up to 17 measurement steps) but becomes increasingly identical related to the decay rate of 33 steps. This means that an improvement of the image quality by decreasing the step size is only possible up to a certain step number because no further improvement of the decay rate can be observed. The reasons are increasing correlations between measurements, which are caused by overlapping eddy current projections. However, one can expect an improvement of the image quality using 33 steps instead of 17 steps only if the MIT system has a low noise level. However, 17 measurement steps were used in this study.

Simulation of sensitivity profile and 2D image reconstruction

The choice of the excitation frequency depends on the skin depth of the eddy currents, which are induced into the specimen. The skin depth δ describes the decrease of the eddy current density in a conductive medium with

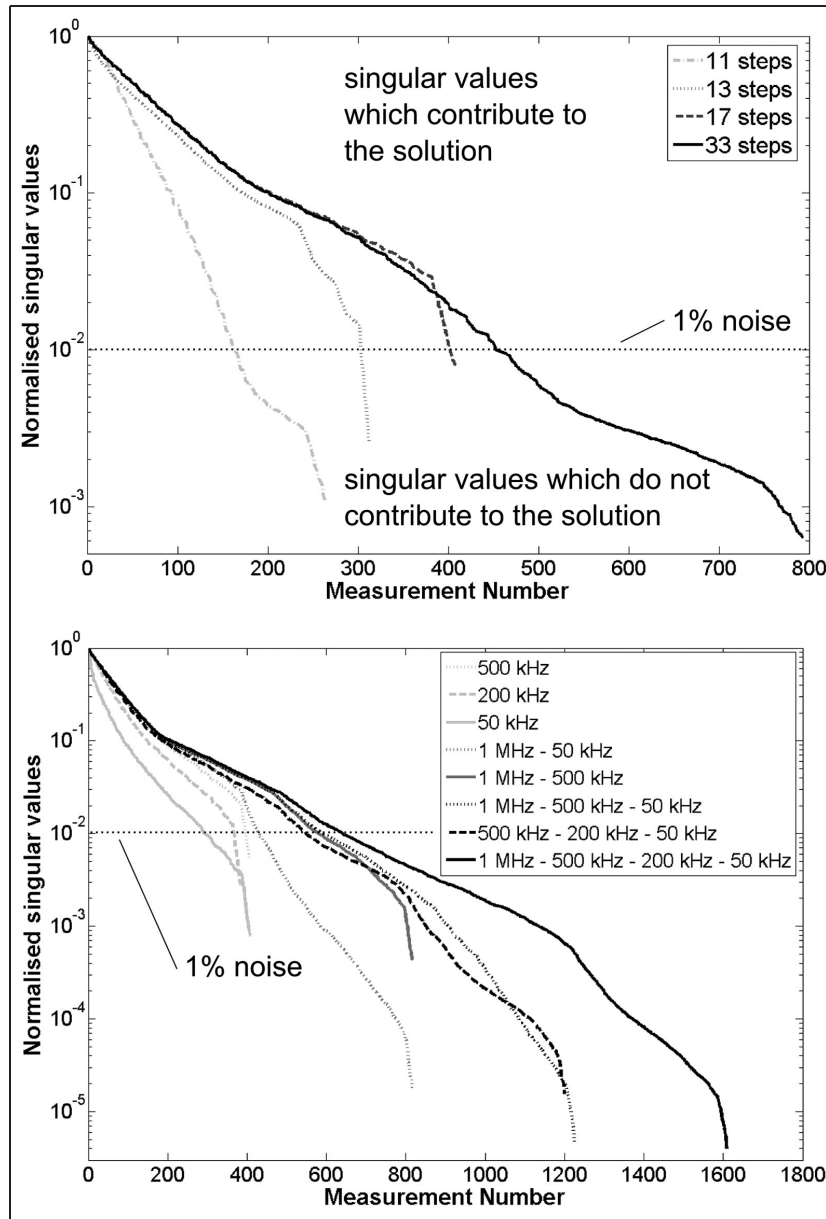


Figure 5. Decay of singular values $SVD(S'S)$ for different counts of steps or excitation frequencies. SVD: singular value decomposition.

depth and is a function of the excitation frequency and the material properties of the specimen's electrical conductivity and magnetic permeability. The skin depth can be calculated (Burke and Rose, 1988) as

$$\delta = \sqrt{\frac{2}{\omega\sigma\mu}} \quad (5)$$

where ω is the angular frequency, $\mu = \mu_0$ is the permeability of free space, and σ is again the conductivity. As can be seen from equation (5), δ decreases with increasing frequencies.

Different skin depths of the eddy currents have in turn an impact on the distribution of the sensitivity

profile. This profile indicates which regions of the specimen contribute to the measurement signal significantly and which do not. The impact of the skin effect can be visualized by computing the sensitivity map, as described before for one and the same coil combination at different excitation frequencies using the FE model of Figure 4(b), and plotting the sensitivity distribution within the specimen. Figure 6 shows the occurring sensitivity profiles within the plate in cross section. For instance, if a frequency of 1 MHz is employed, a low skin depth is given. Consequently, the MIT system is in this case predominantly sensitive to regions, which are near to the surface of the specimen, because eddy currents occur almost exclusively near the surface.

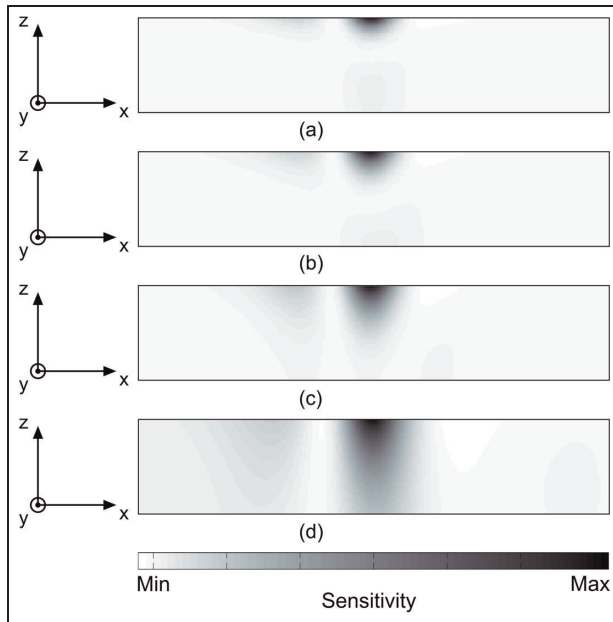


Figure 6. Qualitative cross-sectional sensitivity profile of the 2D imaging problem, which was computed by the FE model in Figure 4(b) for one coil combination at different excitation frequencies of (a) 1 MHz, (b) 500 kHz, (c) 200 kHz, and (d) 50 kHz.

FE: finite element; 2D: two-dimensional.

Otherwise, the MIT system becomes more sensitive to deeper regions of the specimen when lower frequencies (500, 200, or 50 kHz) are used and δ increases (see Figure 6(b) to (d)).

However, the way in which different frequencies affect image reconstruction was studied by means of a 2D imaging problem. Therefore, the arrangement of coils and specimen was modeled cross-sectionally according to the image in Figure 4(b). An inhomogeneity with dimensions of 44 mm in width and 0.975 mm in height was modeled to mimic a material defect in a CFRP specimen. For the modeled CFRP sample, a homogeneous conductivity of 5×10^4 S/m was chosen. The inhomogeneity has a conductivity of 0 S/m. The conductivity distribution of the assembly is shown in Figure 7(a). The measurement vectors were calculated by simulations and charged with 1% noise.

One can see in Figure 7(b) that the inhomogeneity cannot be reconstructed sufficiently regarding its shape and position using a single excitation frequency of 50 kHz. This phenomenon can also be observed by employing *any* excitation frequency. It shows up because the maximum of the sensitivity is always located at the surface of the sample (see Figure 6). As a consequence, the inhomogeneity appears shifted toward the surface of the sample. This effect was reported also in other MIT studies.

To overcome this issue, one needs to assemble more independent data and incorporate depth-related

information into the image reconstruction. This was accomplished by employing a subsequent multifrequency approach. Thereby, measurements at different excitation frequencies were collected sequentially to perform the image reconstruction. Since different excitation frequencies cause different skin depths and eddy current patterns, the reconstruction can be performed with altered sensitivity distributions within the specimen. This improves the condition of the reconstruction problem and hence the image quality.

The advantage of using multiple excitation frequencies can be studied again by investigations of the decay rate of the singular values as described before. Those are shown for this problem in Figure 5(b) for different sensitivity matrices with different frequency combinations. One can clearly see that the decay rate decreases with the count of applied excitation frequencies. Therefore, an improvement of the image quality can be expected for the same reasons as already described.

By reconstructing the simulated 2D images for this arrangement, a significant improvement of the image quality compared to single frequency excitation can already be observed by employing just two frequencies, for instance 200 and 50 kHz (see Figure 7(c)). However, the inhomogeneity was reconstructed more accurate in shape, position, and conductivity compared to the original conductivity distribution when three or four different frequencies were employed (Figure 7(d) and (e)).

Simulated 3D imaging

The topic of 3D imaging of a CFRP plate with regard to the results of the measurement procedure found in the previous sections was studied in simulations first using the numerical model and the coarse imaging mesh. Hence, a square inhomogeneity of $20 \text{ mm} \times 20 \text{ mm} \times 1.4 \text{ mm}$ was modeled with a conductivity of 0 S/m and positioned separately in the middle of each image layer. The measurement vectors were computed by simulations according to the measurement procedure using 17 measurement steps and three excitation frequencies (1 MHz, 200 kHz, and 50 kHz) and were superimposed with 1% random noise subsequently.

Figure 8 illustrates the position of the inhomogeneity within the plate in an isometric view. It also shows the corresponding reconstructed images in the x - y plane as well as the chosen reconstruction parameter λ and the conductivity legends. The reconstructed images clearly demonstrate that the inhomogeneity can be successfully mapped in 3D images within the correct image layer.

The potential of 3D imaging with a higher resolution was investigated by means of a fine imaging mesh. Hence, an inhomogeneity was positioned in the image layers 7–9. Measurement vectors were calculated according to the approach, which was used in imaging

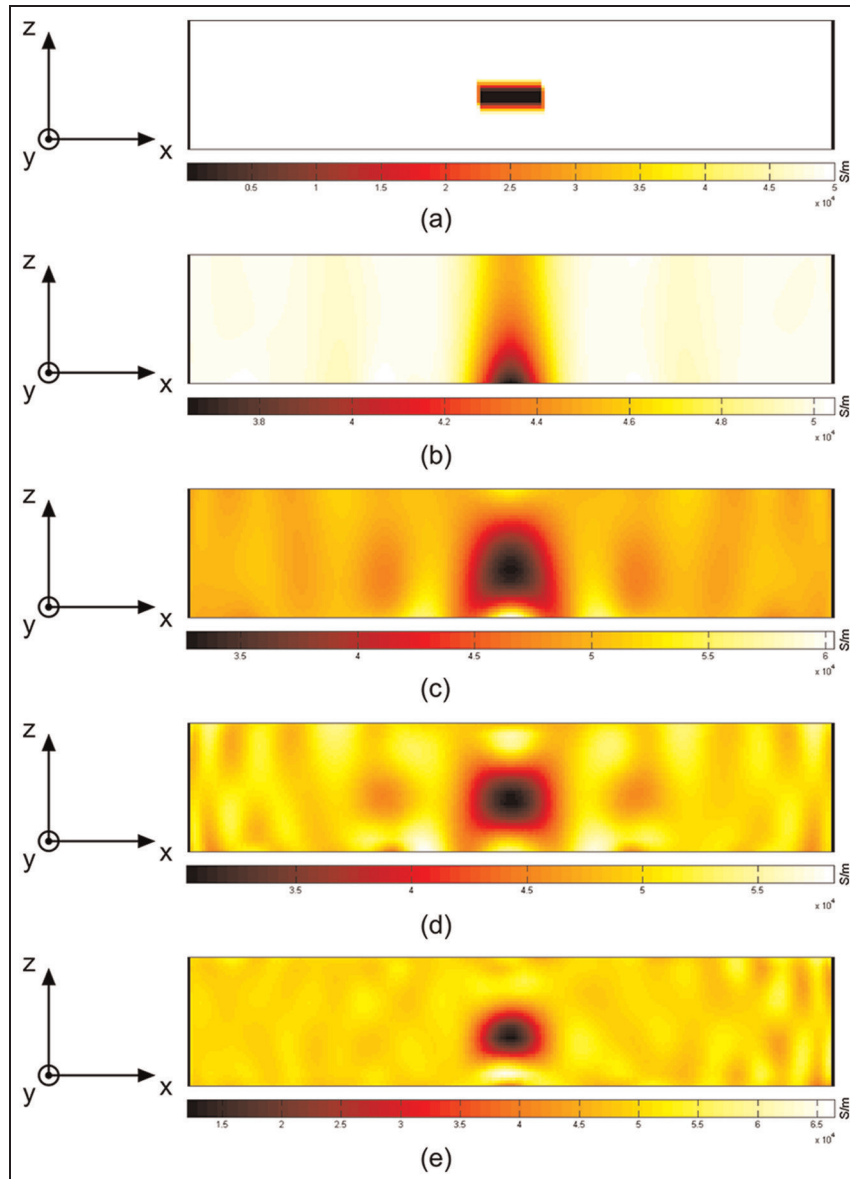


Figure 7. Simulated 2D image reconstruction of (a) a buried inhomogeneity using excitation frequencies of (b) 50 kHz, (c) 200–50 kHz, (d) 1 MHz–200 kHz–50 kHz, and (e) 1 MHz–500 kHz–200 kHz–50 kHz. 2D: two-dimensional.

with the coarse imaging mesh using four excitation frequencies (1 MHz, 500 kHz, 200 kHz, and 50 kHz).

Considering the imaging results (see Figure 11(a)) obtained with this mesh, one can see that the reconstructed images show a minimum of the conductivity in the image layers 7–9. This minimum indicates the depth of the defect. Nevertheless, cross talks into neighboring image layers are clearly visible. This is because the fine imaging mesh has a much higher number of unknowns than the coarse imaging mesh (see Table 1). Consequently, increasing the resolution of the imaging mesh does not necessarily mean that the reconstruction also provides a high resolution.

Preparation of physical experiments for 3D imaging

Two samples were prepared, one for generating a reference data set in undamaged state and the other having a buried inhomogeneity, which mimics the damage. The specimens are 110 mm × 80 mm × 5.6 mm in dimensions and were fabricated by molding. Eight CF2900 woven 2/2 twill fabric prepreg plies (Umeco) were used having a nominal fiber volume content of 52.5%.

To attenuate the effects of anisotropic modeling errors, the cross-ply of the CFRP specimens were assembled in a way that the orientations of the carbon fibers develop approximately quasi-isotropic in-plane conductivity. Hence, the woven plies were assembled in

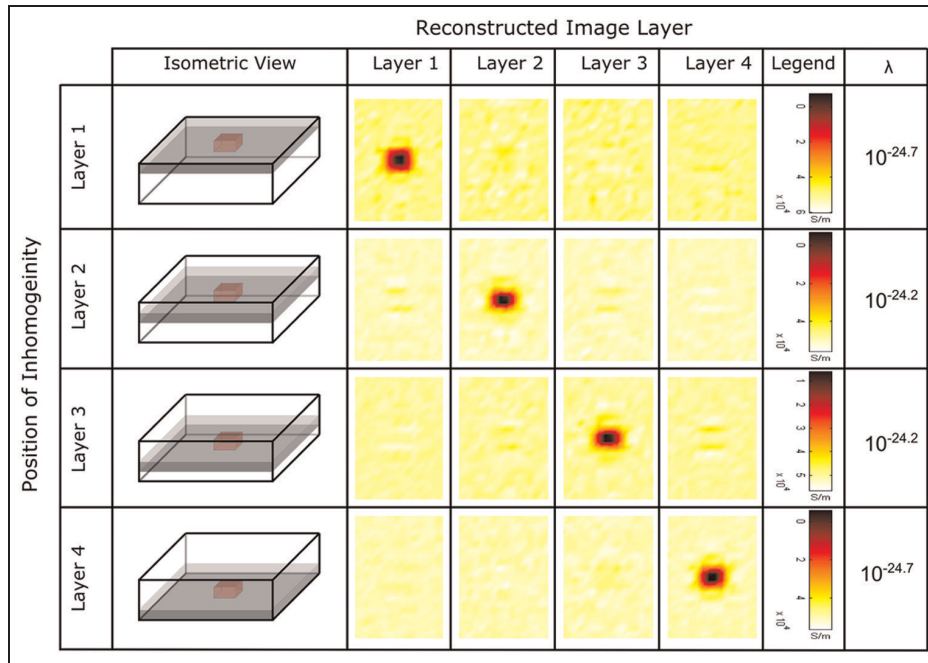


Figure 8. Simulation of 3D imaging of an inhomogeneity, which is positioned in different layers. 3D: three-dimensional.

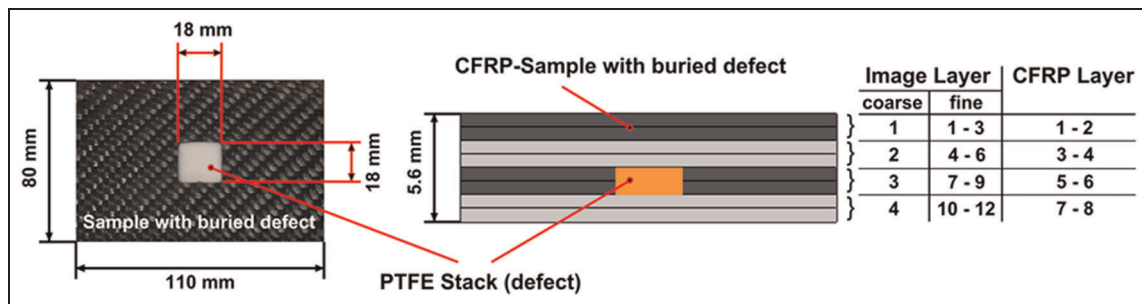


Figure 9. Photograph of the defect layer (left) and illustration of the test specimen in side view (right). CFRP: carbon fiber–reinforced plastic; PTFE: polytetrafluoroethylene.

a sequence of 0°, 45°, 90°, and −45° with a shift in the rotation angle of 45° per layer where the direction of the upper ply (0°) was taken as reference.

To produce a well-defined defect inside the composite, a hole of 18 mm × 18 mm was cut out in prepreg layers 5 and 6 (see Figure 9). To keep the defect area isolated after molding, a stack of polytetrafluoroethylene (PTFE) foils having an overall thickness of 1.4 mm was placed into the hole. The PTFE foils form a perfectly isolating barrier inside the specimen and have a (isotropic) conductivity of 0 S/m similar to the defect modeled for the numerical investigations. The CFRP layer 5 containing the inhomogeneity with the PTFE stack is shown in Figure 9.

Experimental 3D imaging

Considering 3D imaging using the experimental setup and the CFRP specimen having inhomogeneities

positioned in CFRP layers 5 and 6, one would expect those to show up in image layer (1) 3 by using the coarse imaging mesh or (2) 7–9 by using the fine imaging mesh after reconstruction (see Figure 9). Within these experiments, regularization parameters of (1) $\lambda = 10^{-23.1}$ or (2) $\lambda = 10^{-24.9}$ were chosen. The results of the reconstruction are presented in Figures 10 and 11(b).

The inhomogeneity can be clearly identified within the expected image layer(s) in both cases but its aspect ratio deviates from that of the produced defect as well as the numerically reconstructed flaw and appears obviously blurred and as long drawn structure. Reasons for this discrepancy between numerical and experimental results are that the measurements used for experimental reconstructions are erroneous due to noise and drift and position errors made by swapping of the specimen. Further errors may be introduced due to anisotropic modeling errors as mentioned before. All in all, these

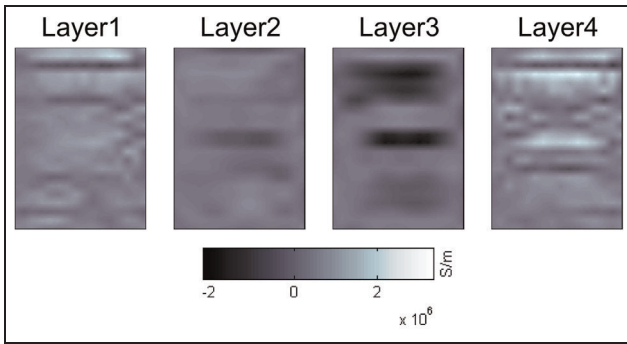


Figure 10. Experimental results of 3D imaging of a CFRP specimen with a buried defect using the coarse imaging mesh. CFRP: carbon fiber–reinforced plastic; 3D: three-dimensional.

errors exceeded the error assumption of 1% random noise made for the numerical reconstruction. The lamellar form could also be a consequence of the sensitivity profile, which is in turn dependent on the

assembly of excitation and detection coils. In this study, it shows long drawn sensitivity maps in the setup used. Choosing a higher number of steps could be an option to overcome this issue. For instance, image reconstruction executed with 33 steps might already map the defect more accurate in shape. Another option is to improve the coil arrangement or using measurements with multiple coil combinations.

Using the coarse imaging mesh, just very little cross talk into image layers 2 and 4 can be observed. Anyway, more cross talk into neighboring image layers can be noted using the fine imaging mesh for reconstruction. Furthermore, the defect seems to be shifted toward the center of the specimen in this case. In comparison to the simulation (see Figure 11), the defect expected in layer 9 is marginally visible but shows up in layer 6 where it is not expected. There are two possibilities for explanation. First, the absolute depth position of the PTFE stack within the specimen is not exactly

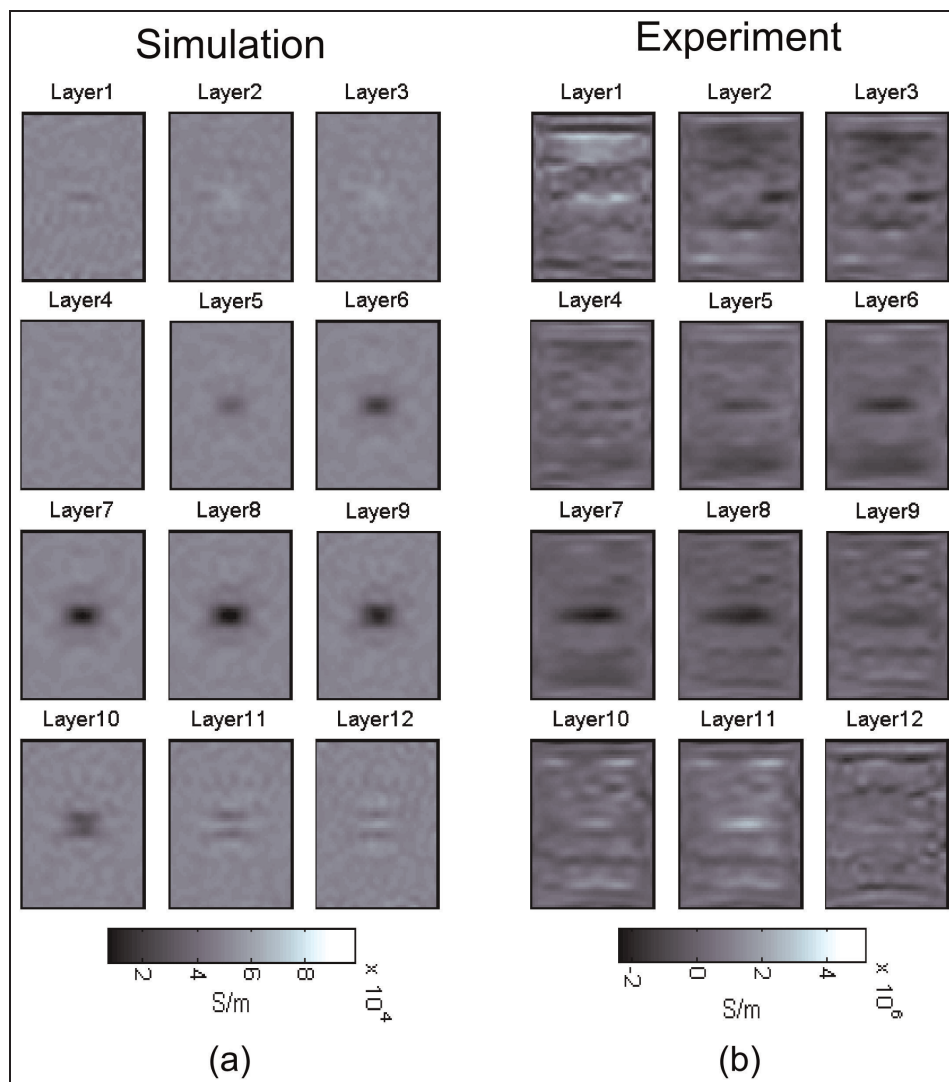


Figure 11. 3D imaging of a CFRP specimen with a buried defect using the fine imaging mesh in (a) simulations and (b) experiments. CFRP: carbon fiber–reinforced plastic; 3D: three-dimensional.

known, and second, this could also be a consequence of erroneous data mentioned in the previous paragraph.

However, the absolute conductivities of the reconstructed images do not agree with the physics because a difference imaging approach was applied. The sharp edges of the inhomogeneity could not be recovered since Tikhonov regularization produces always smooth images. A recently published study demonstrates that a further improvement of blocky images with sharp edges can be achieved by applying total variation regularization instead of Tikhonov's regularization (Yin et al., 2011).

Conclusion

A novel inexpensive and contactless imaging method for NDE of conductive FRPs was presented, which combines the advantages of conventional eddy current testing and tomography methods. FE simulations as well as physical experiments showed that an inhomogeneity, which is buried inside the considered CFRP specimen, can be successfully found and mapped in 3D images with good spatial resolution. Considering the experimental results of 3D imaging, a resolution in depth in the order of almost millimeter size was achieved, which was not reported yet in MIT studies.

Numerical studies concerning 2D imaging have shown that one can achieve a good spatial resolution by employing different excitation frequencies. Anyway, there are some other options to increase the image quality. For instance, one can improve the coil arrangement or use measurements with different coil combinations.

The presented imaging approach might become more attractive in NDE applications if image reconstruction would require only single-sided data collection since only one surface of the specimen needs to be accessible for measurement acquisition. Numerical investigations performed by the authors agreed with Watson et al. (2005), which have shown that single-sided imaging is possible in a noise-free and error-free environment. Within realistic conditions, this will be harder to accomplish and a careful design of the overall MIT system will be necessary.

A reconstruction of the absolute conductivity should be possible by applying a nonlinear reconstruction approach, which would enable the estimation of the severity of damages. The anisotropic conductivity distribution of FRPs will be incorporated into the future study using an anisotropic reconstruction solver, which probably improves the image quality and would make it possible to distinguish between different kinds of damages like fiber fracture or delamination.

The presented MIT setup can be used in autonomous SHM of conductive composites, when the transceivers as well as the electronics become miniaturized for composite integration or superficially attachment.

Such a system would allow in situ tomography even during operation of a composite part. Furthermore, the 4D imaging approach presented by Wei and Soleimani (2012a) could be very attractive in SHM applications and could be used for time-resolved visualization of events like damage development or cyclic opening and closing of cracks. Furthermore, local temperature changes, which could be caused, for instance, due to friction loss at delaminations, will also cause conductivity changes. However, the reconstructed data might be used for detailed diagnostic statements, which would give an input for a regulating actuator system to realize smart structures.

Acknowledgements

The authors would like to thank the Center of Information Services and High Performance Computing of the TU-Dresden for the allocation of computing time.

Declaration of conflicting interests

The authors declare that there is no conflict of interest.

Funding

This study was financially supported by the European Union and the Free State of Saxony, which was accomplished in the framework of the cluster of excellence "European Centre for Emerging Materials and Processes Dresden (ECEMP)."

References

- Abrý JC, Choi YK, Chateauminois A, et al. (2001) In-situ monitoring of damage in CFRP laminates by means of AC and DC measurements. *Composites Science and Technology* 61: 855–864.
- Baltopoulos A, Polydorides N, Vavouliotis, et al. (2010) Sensing capabilities of multifunctional composite materials using carbon nanotubes. In: *61st international astronautical congress*. 27 September–1 October 2010, Prague, Czech Republic.
- Böger L, Wichmann MHG, Meyer LO, et al. (2008) Load and health monitoring in glass fibre reinforced composites with an electrically conductive nanocomposite epoxy matrix. *Composites Science and Technology* 68: 1886–1894.
- Burke SK and Rose LRF (1988) Interaction of induced currents with cracks in thin plates. *Proceedings of the Royal Society A: Mathematical Physical and Engineering Sciences* 418: 229–246.
- Griffiths H (2001) Magnetic induction tomography. *Measurement Science & Technology* 12: 1126–1131.
- Gürsoy D and Scharfetter H (2009) The effect of receiver coil orientations on the imaging performance of magnetic induction tomography. *Measurement Science & Technology* 20: 1–9.
- Gürsoy D and Scharfetter H (2010) Anisotropic conductivity tensor imaging using magnetic induction tomography. *Physiological Measurement* 31: 135–145.
- Hanke M and Hansen PC (1993) Regularization methods for large-scale problems. *Surveys on Mathematics for Industry* 3: 253–315.

- Hollaus K, Magele C, Merwa, et al. (2003) Fast calculation of the sensitivity matrix in magnetic induction tomography by tetrahedral edge finite elements and the reciprocity theorem. *Physiological Measurement* 25: 159–168.
- Kostopoulos V, Vavouliotis A, Karapappas P, et al. (2009) Damage monitoring of carbon fiber reinforced laminates using resistance measurements. Improving sensitivity using carbon nanotube doped epoxy matrix system. *Journal of Intelligent Material Systems and Structures* 20: 1025–1034.
- Kupke M, Schulte K and Schüller R (2001) Non-destructive testing of FRP by d.c. and a.c. electrical methods. *Composites Science and Technology* 61: 837–847.
- Lane SS, Moore RH, Groger HP, et al. (1991) Eddy current inspection of graphite/epoxy laminates. *Journal of Reinforced Plastics and Composites* 10: 158–166.
- Li X (2012) *Eddy current techniques for non-destructive testing of carbon fibre reinforced plastic (CFRP)*. PhD Thesis, The University of Manchester, Manchester.
- Ma X, Peyton AJ, Higson SR, et al. (2006) Hardware and software design for an electromagnetic induction tomography (EMT) system applied to high contrast metal process applications. *Measurement Science & Technology* 17: 111–118.
- Merwa R, Hollaus K, Brunner P, et al. (2005) Solution of the inverse problem of magnetic induction tomography (MIT). *Physiological Measurement* 26: 241–250.
- Ngabonziza Y, Ergun H, Kuznetsova R, et al. (2010) An experimental study of self-diagnosis of interlaminar damage in carbon-fiber composites. *Journal of Intelligent Materials Systems and Structures* 21: 233–242.
- Peyton AJ, Yu ZZ, Al-Zeibak S, et al. (1995) Electromagnetic imaging using mutual inductance tomography: potential for process applications. *Particle & Particle Systems Characterization* 12: 68–74.
- Schüller R, Joshi SP and Schulte K (2001) Damage detection in CFRP by electrical conductivity mapping. *Composites Science and Technology* 61: 921–930.
- Soleimani M (2005) *Image and shape reconstruction methods in magnetic induction and electrical impedance tomography*. PhD Thesis, University of Manchester, Manchester.
- Soleimani M and Lionheart WRB (2006) Absolute conductivity reconstruction in magnetic induction tomography using a nonlinear method. *IEEE Transactions on Medical Imaging* 25: 1521–1530.
- Soleimani M, Lionheart WRB, Peyton AJ, et al. (2006) A three-dimensional inverse finite-element method applied to experimental eddy-current imaging data. *IEEE Transactions on Magnetics* 42: 1560–1567.
- Todoroki A (2008) Delamination monitoring analysis of CFRP structures using multi-probe electrical method. *Journal of Intelligent Materials Systems and Structures* 19: 291–298.
- Watson S, Igney CH, Dössel O, et al. (2005) A comparison of sensors for minimizing the primary signal in planar-array magnetic induction tomography. *Physiological Measurement* 26: 319–331.
- Wei H-Y and Soleimani M (2012a) Four dimensional reconstruction using magnetic induction tomography: experimental study. *Progress in Electromagnetics Research: PIER* 129: 17–32.
- Wei H-Y and Soleimani M (2012b) Two-phase low conductivity flow imaging using magnetic induction tomography. *Progress in Electromagnetics Research: PIER* 131: 99–115.
- Wei H-Y and Soleimani M (2012c) Theoretical and experimental evaluation of rotational magnetic induction tomography. *IEEE Transactions on Instrumentation and Measurement* 61: 3324–3331.
- Wei H-Y, Ma L and Soleimani M (2012) Volumetric magnetic induction tomography. *Measurement Science & Technology* 23: 1–9.
- Yang CQ, Wu ZS and Huang H (2007) Electrical properties of different types of carbon fiber reinforced plastics (CFRPs) and hybrid CFRPs. *Carbon* 45: 3027–3035.
- Yin W, Chen G, Chen L, et al. (2011) The design of a digital magnetic induction tomography (MIT) system for metallic object imaging based on half cycle demodulation. *IEEE Sensors Journal* 11: 2233–2239.